Geophysical Journal International

Geophys. J. Int. (2011) **186,** 706–710 doi: 10.1111/j.1365-246X.2011.05063.x

EXPRESS LETTER

A stagnant slab in a water-bearing mantle transition zone beneath northeast China: implications from regional *SH* waveform modelling

Lingling Ye,[1] Juan Li,[1] Tai-Lin Tseng[2] and Zhenxing Yao[3]

[1] *Key Laboratory of the Earth's Deep Interior, Institute of Geology and Geophysics, Chinese Academy of Sciences, Beijing, China. E-mail: juanli@mail.iggcas.ac.cn*

[2] *Department of Geosciences, National Taiwan University, Taipei, Taiwan*

[3] *Institute of Geology and Geophysics, Chinese Academy of Sciences, Beijing, China*

Accepted 2011 April 29. Received 2011 April 24; in original form 2010 October 9

SUMMARY

SH waveforms recorded by a dense regional seismic network are used to constrain the shear wave velocity structure of the upper-mantle transition zone beneath northeast China. By modelling triplication waveforms we show that a 130-km-thick layer of increased seismic velocities is overlying a broad slightly depressed 660 km discontinuity. This anomaly can be associated with the westward extension of the stagnant Pacific slab that is deflected and still cold. The transition zone, as a whole, is featured by low shear wave velocity and high V_p/V_s ratio, which infer H_2O content of ~0.2–0.3 wt. per cent [$(3.0–4.5)\times10^4$ ppm H/Si] atop the 660 km discontinuity. We interpret that the fast eastward retreat of the Japan Trench facilitated the slab flattening when the subducting oceanic lithosphere hit the bottom of the transition zone, and the leading edge of the slab is currently trapped in a water-bearing mantle beneath northeast China.

Key words: Body waves; Subduction zone processes; Pacific Ocean.

GJI Seismology

1 INTRODUCTION

The seismic structure of the upper-mantle transition zone (MTZ) is fundamentally important for understanding the scales of mantle circulation as well as the composition of the upper mantle. The 660-km discontinuity (hereafter referred to as the 660), a phase boundary, plays an important role in determining the fate of subducted lithosphere. The undulation of the 660 is generally believed to be caused by thermal anomalies, and a temperature-induced depression of the 660 is expected in the subduction areas due to the negative Clapeyron slope of postspinel transformation (e.g. Ito & Takahashi 1989). Non-olivine phase transitions, major element addition or water content, however, can result in a complicated morphology and velocity structure around the 660 (e.g. Niu & Kawakatsu 1996; Jacobsen & Smyth 2006; Schmerr & Garnero 2007).

Subduction zones in the northwestern Pacific are widely studied and a variety of tomographic images can be found in the literature. A sharp horizontal deflection of the subducted slab above the 660 beneath Japan and Izu-Bonin arcs has been mapped by *P*-wave traveltime tomography (Van Der Hilst *et al.* 1991; Fukao *et al.* 2001; Huang & Zhao 2006); while a slab directly penetrating into the lower mantle is also detected beneath Japan by global *P*-wave tomography (Bijwaard *et al.* 1998). A joint bulk-sound and shear wave traveltime inversion reveals substantial differences in the stagnant slab images between the two types of tomography images beneath the Izu-Bonin arc (Widiyantoro *et al.* 1999; Gorbatov & Kennett 2003). The discrepancy of tomography images is partly due to poor ray coverage of the first arrivals in the deeper portion of the MTZ (Tajima & Grand 1995).

As an alternative approach, triplicate *P* or *S* seismic waveforms in regional distances can be modelled to constrain MTZ velocity structure effectively (e.g. Tajima *et al.* 2009). The triplication waveforms include three sets of arrivals, representing the waves propagating above the discontinuity (AB), the wide-angle reflection off the discontinuity (BC) and the waves diving below the discontinuity (CD) (inset of Fig. 1). Since ray paths of the three arrivals associated with the 660 are very close to each other in the crust and uppermost mantle, the relative time interval and amplitude between the two phases are primarily sensitive to the velocity structure near the 660. However, results of recent studies revealed considerable differences in velocities of the MTZ for regions adjacent to each other beneath the northwestern Pacific subduction zone (e.g. Tajima & Grand 1995; Wang *et al.* 2006; Wang & Chen 2009; Wang & Niu 2010), yielding ambiguous interpretations about the structure and composition of the deep upper mantle. In this study, we report new results from modelling of the regional *SH* wavefield from a dense seismic array to constrain the MTZ structure beneath northeast China west of the Japan subduction zone (Fig. 1). The resolved shear wave velocity structure might give new clues to compositional and/or thermal anomaly identification, and for an understanding of the

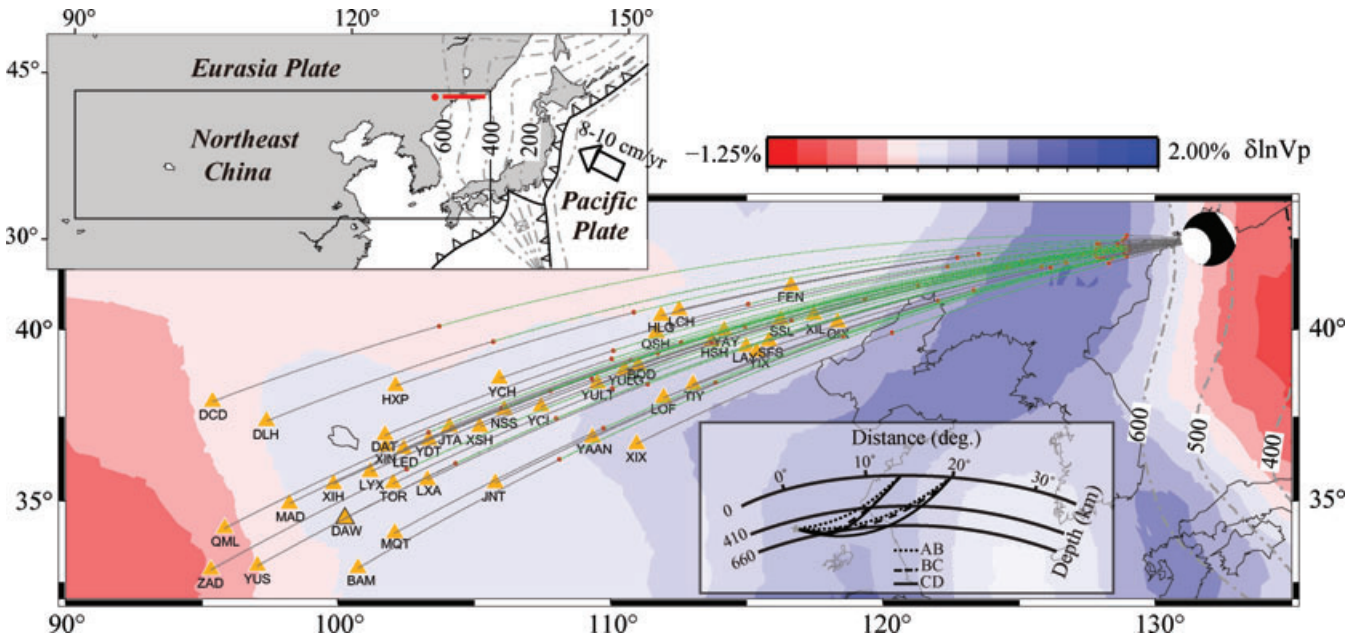

Figure 1. Map showing the location of earthquake and regional stations used in this study. The great circle paths connecting the event and seismic stations (yellow triangle) are shown by black curves, along which the green segments bounded by two red dots highlight the portions of CD phases travelling below the 660. The *P*-wave velocity perturbation in the depth range of 629–712 km from Fukao *et al*. (2001) is shown as background. The upper-left inset shows the study region within the Eurasia plate and the subducting northwestern Pacific plate. The Wadati–Benioff zone is indicated by dash-dotted contours. The red dot in the inset marks the region with a local maximum depression of 35 km in the 660-km discontinuity from receiver function analysis (Li & Yuan 2003). The red line indicates a profile of constrained 660 topography based on the study of source-side *S*-to-*P* converted waves (Li *et al*. 2008). The 660 gradually deepens to the west with the maximum depression of ∼20 km beneath the west end of the profile. The inset at the bottom is a schematic diagram of seismic triplication with ray path of three phases: AB—waves propagating above the 660; BC—waves reflected off the 660; CD—waves diving below the 660.

dynamic processes beneath the westward portion of the subducting Pacific slab.

2 DATA AND OBSERVATIONS

In this study, we used broad-band waveforms collected from dense regional seismic networks in China installed in 2007 (Zheng *et al*. 2010). To avoid spatial aliasing, we selected a total of 43 stations within a very narrow azimuth range of 257–270° for a moderate-sized deep event occurring offshore the border between east Russia and northeast China (PDE (Preliminary Determination of Epicenters) location: 42.5°N, 131.87°E, depth = 522 km, 2008 May 19, $M = 5.7$) . The turning points of the directed and refracted rays sample the MTZ extensively west of the Japan trench (Fig. 1), allowing a tight constraint in velocity near the 660 beneath the northwestern Pacific subduction zone. Since the focal depth is crucial for estimating the upper-mantle velocities, we redetermined the focal depth to be about 519 ± 3 km by measuring 330 pairs of manually picked *pP* and *P* arrival times on teleseismic records (see Fig. S1 and Supplement S1 of Supporting Information). Such a deep focus also effectively avoids signals of the 660 triplication be further contaminated by arrivals from shallower discontinuities.

To model triplicate waveforms in high resolution, we first removed the instrument responses from all records on the transverse component, and then applied a bandpass filter of 0.04–0.5 Hz, which preserves the dominant frequency of shear waves. When plotting the *SH* waveforms against the epicentral distances, we noted that the first *S* arrivals are generally delayed by 2.0–4.0 s comparing to the theoretical traveltimes calculated from the global standard model iasp91 (Kennett & Engdahl 1991, Fig. 2a). To compensate the time difference resulting mainly from the shallow structure above the 410-km discontinuity, we followed Tajima & Grand (1998) and Wang & Chen (2009), who modified the velocity structure above 410 km according to Fukao (1977) (See model Miasp in Figure S2). The velocities deeper than 410 km are further constrained by the modelling of the observed triplication.

Main features in the 660 triplication offer critical clues to the velocities near the discontinuity. The *SH* triplication branches can be clearly identified in a distance range of 13–25° (Fig. 2a). The AB branch likely extends out to much further distances of approximately 25° as indicated by the onset of diminishing amplitudes. This termination distance, cusp B, is sensitive to the lower MTZ right above the 660. The CD branch begins to emerge at ∼13° and crosses over the AB branch at ∼16° where the waveforms are most compact (point O). Starting at distances of about 13°, the CD arrivals reach the top of the lower mantle and bottom successively deeper to a depth of ∼770 km as the distance increases to ∼25°. We found that the 'BOD', confined by the intervals between AB and CD phases, is particularly broad with a significantly delayed AB after distance ∼18°. Such striking features cannot be explained by either the iasp91 model, or the regional models obtained from previous waveform modelling (e.g. models 'M3.11' (Tajima & Grand 1998), 'Asia' (Wang *et al.* 2006), 'Japan' (Wang & Chen 2009) and '255–270' (Wang & Niu 2010) in Supporting Information Fig. S7.

3 RESULTS OF MODELLING AND IMPLICATIONS

We applied the 1-D reflectivity synthetic code (Fuchs & Muller 1971; Wang 1999) in generating theoretical seismograms to fit observed waveforms. We took source mechanism from Global CMT

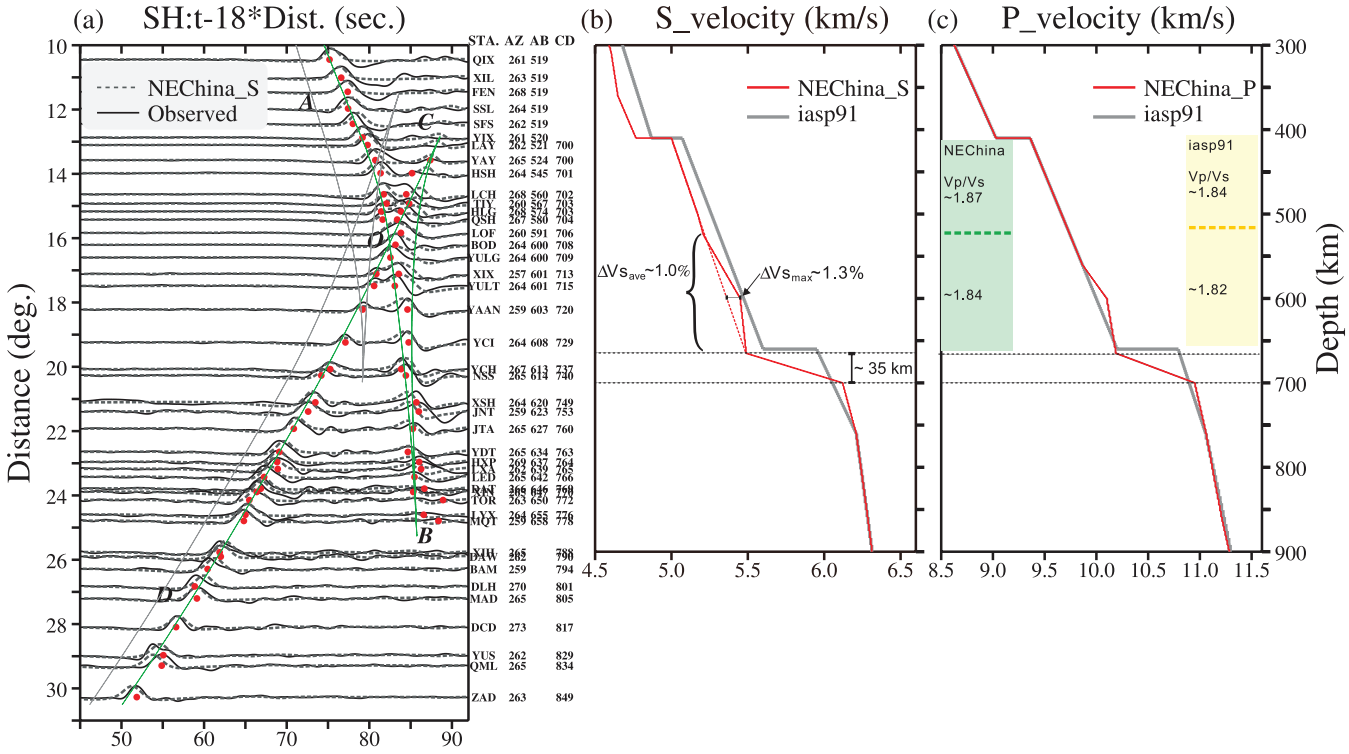

Figure 2. (a) Comparison of observed transverse displacements (black lines) and synthetic waveforms (dashed lines) calculated using our preferred model—'NEChina_S'. The theoretical traveltime curves of this model calculated by TauP (Buland & Chapman 1983) are plotted as green curves; while the grey curves are the prediction from model iasp91. The red dots mark the picked arrival time for the peaks of AB and CD phases. (b) Comparison of the *S* velocity models of iasp91 and our preferred model 'NEChina_S'. (c) Comparison of the *P* velocity models of iasp91 and our preferred model 'NEChina_P'. Station corrections of ∼2.0 s are made for seven stations located within epicentral distance 18°–22°, which might be related with the local structure beneath stations. The four numbers at the right side of each waveform in (a) represent the name and azimuth angle of each station, the bottoming depths of the AB and CD phases calculated from model 'NEChina_S', respectively.

(Dziewonski *et al.* 1981), and used a Gaussian wavelet to represent the source time function as indicated by the simple teleseismic waveform. We determine the optimal depth of the 660 and the velocity gradients above and below the discontinuity by forward modelling (systematic tests available in Supporting Information), which is guided by our qualitative understanding of the detected features. For each model, we calculated the coefficient of cross-correlation between the synthetic and observed waveforms to determine the goodness of fit. To match the extended cusp B to a distance of ∼25° in contrast to ∼20° in iasp91/Miasp without shifting the crossover distance of point O, we found that the gradient of V_s in the lower MTZ must be very gentle. Moreover, the shortened CO branch, corresponding to rays turning just below the 660, suggests a slightly depressed and broad 660-km discontinuity. The large time interval between AB and CD phases (i.e. broad 'BOD') could be matched by a reduced velocity structure above the 660 (Fig. 2). It should be noted that the velocity structure above the focal depth, are obtained mainly from the absolute traveltime fits of AB, and thus is less well constrained. However, the velocity structure below the earthquake is well constrained by both the traveltimes and waveforms associated with the 660-km triplication.

Our preferred shear velocity model 'NEChina_S' shows the presence of a relatively high velocity (∼1 per cent) anomaly with thickness of ∼130 km lying above the 660, which is depressed slightly to 665 km (Fig. 2b). The overall feature of the high velocity layer in the MTZ is in agreement with tomographic images (Huang & Zhao 2006; Van Der Hilst *et al*. 1991) in which a horizontally deflected fast V_p anomaly extends westwards for ∼800–1000 km under Korea Peninsula and NE China. We also found that the 660 is broad, a ∼35-km-thick transition with a large V_s jump across the boundary, which is consistent with the latest V_p result of Wang & Niu (2010) for the same area. The depth of the 660 in our 'NEChina_S', however, is considerably shallower than that determined by previous studies in nearby regions. A 30-km depressed discontinuity as in *P*-velocity model 'M3.11' proposed by Tajima & Grand (1998) can be readily rejected by the mismatch of observed large move out between AB and CD branches and position of their crossover point O (Figure S7b). Wang *et al*. (2006) modelled the *SH* waveform beneath northeast China using a large aperture array, and suggested an even deeper 660-km discontinuity at 730 km. However, such a large depression would result in a further terminal distance of AB phase at ∼32°, which is inconsistent with our observation (Figure S7b). We argue that limitation of the earlier data, error estimation in focal depth, lateral variation of the MTZ, and subtle effects of variation in physical properties on *P* and *S* velocities, might contribute to the discrepancy.

The observed V_s anomaly may be converted to a difference in temperature if the velocity variations are purely induced from thermal origin. Based on the 1-D velocity profile of 'NEChina_S' (Fig. 2b), we first identify that the maximum velocity anomaly relative to the trend of the velocity throughout the MTZ to be ∼1.3 per cent, which occurs at depth of around 600 km. The average anomaly in the lower ∼130 km of the MTZ is about 1 per cent. Taking the temperature derivative of –6 to –7 × 10^{-5} K^{-1} for shear wave velocity (Cammarano *et al.* 2003), we can then calculate the corresponding temperature deficit to be around 143–166 K. Since the Clapeyron

slope of the phase decomposition of ringwoodite around the 660 is between –2.0 and –3.0 MPa K^{-1} (Bina & Helffrich 1994; Litasov *et al.* 2005), we expected the 660-km discontinuity be depressed by about 8–10 km, which is also consistent with our preferred model 'NEChina_S'.

A number of experimental studies imply the presence of water in the slab and the surrounding MTZ (e.g. Karato 2011). Water in the MTZ can be stored in wadsleyite and ringwoodite up to 3 wt. per cent (Bercovici & Karato 2003), resulting in a reduced shear velocity and increased V_p/V_s ratio. To characterize the variation of Poisson's ratio in this region, we go through another round of *P*-wave analysis using the same pair of station–event geometry as in the *S*-wave study. Our preferred V_p model 'NEChina_P' (Fig. 2c) is almost identical to that of Wang & Niu (2010), despite one minor difference in the sharpness of the 660. Unlike the overall slow V_s in the MTZ relative to iasp91 in the 'NEChina_S', the corresponding *P*-wave velocity seems to be quite 'normal' as a whole. We estimate the V_p/V_s ratio of the upper MTZ and the anomalously fast lower part to be ∼1.87 and ∼1.84, respectively, higher than the values of 1.84 and 1.82 in the global average model iasp91. Pure thermal effects could not explain the discordance between variations in V_p and V_s; while effect of major element geochemistry seems to be complex and difficult to reconcile (Higo *et al.* 2006). One simple and possible explanation is the presence of hydroxyls that structurally corporate into mantle minerals (Jacobsen & Smyth 2006; Jacobsen *et al*. 2004). The laboratory experiment on Fe-bearing ringwoodite indicates that adding 0.1 wt. per cent H_2O can reduce shear wave velocity by about 0.04 km s^{-1} at lower transition zone condition (Jacobsen *et al.* 2004). Based on those findings and the V_s reduction of 0.08–0.12 km s^{-1} in our 'NEChina_S' relative to iasp91, we propose that a possible water content of ∼0.2–0.3 wt. per cent H_2O [(3.0–4.5) × 10^4 ppm H/Si] exists in the MTZ.

Fukao (2009) argued that subducted slabs generally tend to be horizontally flattened between the depth of 400 and 1000 km. The subducting slab is deflected horizontally when the downgoing part hits the bottom of the upper mantle, where the great depression of the 660 is expected. Li & Yuan (2003) detected a maximum depression of ∼35 km to the northeast corner of our sampled region where the downgoing slab reaches the bottom of the MTZ (red dot, inset of Fig. 1). Slightly further to the east, a gentle decrease of the depressed 660-km discontinuity from depth of 680 km to 665 km is revealed by (Li *et al.* 2008) who used the source-side *S*-to-*P* converted wave to map out detailed changes of the 660 topography (red line, inset of Fig. 1). From the degree of the 660 depression, we speculate that along the 660-km discontinuity, it is coldest in the bottoming part of the downgoing slab, corresponding to an anomaly of ∼ –400 K; while it is less cold in the flattened part westwards, where our study region is mainly focused (Fig. 3). Combined with the tomographic images beneath north China (Huang & Zhao 2006), our results imply that the stagnant Pacific slab lies subhorizontally in a water-bearing MTZ beneath northeastern China (Fig. 3). The east margin of the water-bearing MTZ, however, is difficult to constrain due to the spatial coverage of the array. The deduced ∼0.2–0.3 wt. per cent water content might not be distributed uniformly between the MTZ itself and the surrounding slab. Nevertheless how water is transported and stored in the MTZ is still a question for further investigation.

Overall, our results are consistent with the hypothesis that the near-horizontal deflection of subducted slab could be caused by the eastward migration of the Japan Trench. Numerical models found that trench migration tends to prevent slab penetration into the lower mantle and to facilitate the slab flattening above the phase boundary. The rapid trench migration, under Japan-Kurile arc from Miocene revealed by palaeotectonic reconstruction studies (Miller *et al.* 2006), might create a shallow dip angle and result in a horizontally deflected slab extending westwards over a long distance in the MTZ beneath northeast China.

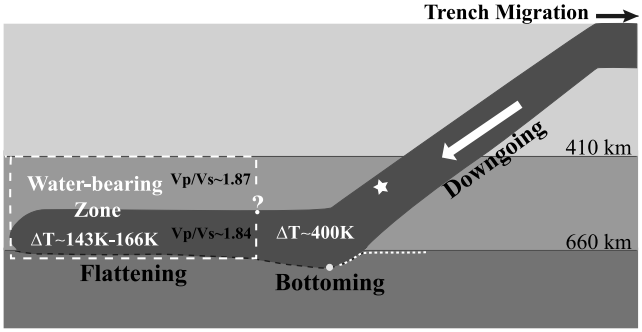

Figure 3. A schematic cross-section illustrating the eastward retreat scenario of subducting Pacific slab with its downgoing, bottoming and flattening parts. The white rectangle roughly corresponds to the region of high V_p/V_s ratio and overall low V_s, implying the MTZ is water bearing. The flattening slab with slightly colder temperature is inferred from relatively high velocities constrained near the bottom of the MTZ. The black dashed line shows the expected topography of the 660 inferred from our study. The white dashed line along the 660 is defined based on the depth of conversion points obtained from study of *S*-to-*P* conversion wave (Li *et al*. 2008). The white dot marks the location of the deepest 660 constrained by receiver functions (Li & Yuan 2003). Star indicates the location of the deep earthquake used in this study.

4 CONCLUSIONS

Our results indicate a high-velocity anomaly in the deeper part of a water-bearing MTZ. There is a broad 660-km discontinuity with a slight depression beneath the study region, implying a limited temperature anomaly beneath the westward extended stagnant slab. The integrated picture of the slab and the undulation of the 660 support a scenario that the slab is not penetrating directly into the lower mantle, but rather lying horizontally above the 660, which might be due to the eastward retreat of the Japan Trench. Nevertheless, for a full understanding of the geodynamic mechanism and composition of the MTZ beneath the northwestern Pacific subduction zone, finite difference synthetic scheme for a 3-D velocity structure should be applied in the modelling to account for the lateral variation, and a joint *P* and *S* waveform modelling with the same receiver–source geometry for a larger aperture is required.

ACKNOWLEDGMENTS

We thank the Data Management Centre of China National Seismic Network at Institute of Geophysics, China Earthquake Administration for providing seismic waveform data. We thank S. Rost and an anonymous reviewer for constructive suggestion and comments, which greatly improve the manuscript. We thank F. Niu for useful discussion and W. Jacoby for grammatical correction. This work was supported by the NSFC (grants 41074034, 40774042 and 90714012), and NSC (grant 99-2116-M-002-006-MY2).

REFERENCES

Bercovici, D. & Karato, S., 2003. Whole-mantle convection and the transition-zone water filter, *Nature,* **425,** 39–44.

Bijwaard, H., Spakman, W. & Engdahl, E.R., 1998. Closing the gap between regional and global travel time tomography, *J. geophys. Res.,* **103,** 30 055–30 078.

Bina, C.R. & Helffrich, G., 1994. Phase-transition Clapeyron slopes and transition zone seismic discontinuity topography, *J. geophys. Res.,* **99,** 15 853–15 860.

Buland, R. & Chapman, C.H., 1983. The computation of seismic travel times, *Bull. seism. Soc. Am.,* **73,** 1271–1302.

Cammarano, F., Goes, S., Vacher, P. & Giardini, D., 2003. Inferring upper-mantle temperatures from seismic velocities, *Phys. Earth planet. Inter.,* **138,** 197–222.

Dziewonski, A.M., Chou, T.A. & Woodhouse, J.H., 1981. Determination of earthquake source parameters from waveform data for studies of global and regional seismicity, *J. geophys. Res.,* **86,** 2825–2852.

Fuchs, K. & Muller, G., 1971. Computation of synthetic seismograms with the reflectivity method and comparison with observations, *Geophys. J. R. astr. Soc.,* **23,** 417–433.

Fukao, Y., 1977. Upper mantle P structure on the ocean side of the Japan-Kurile arc, *Geophys. J. Int.,* **50,** 621–642.

Fukao, Y., Widiyantoro, S. & Obayashi, M., 2001. Stagnant slabs in the upper and lower mantle transition region, *Rev. Geophys.,* **39,** 291–323.

Fukao, Y., Obayashi, M., Nakakuki, T. & Grp, D.S.P., 2009. Stagnant slab: a review, *Annu. Rev. Earth planet. Sci.,* **37,** 19–46.

Gorbatov, A. & Kennett, B.L.N., 2003. Joint bulk-sound and shear tomography for Western Pacific subduction zones, *Earth planet. Sci. Lett.,* **210,** 527–543.

Higo, Y., Inoue, T., Li, B.S., Irifune, T. & Liebermann, R.C., 2006. The effect of iron on the elastic properties of ringwoodite at high pressure, *Phys. Earth planet. Inter.,* **159,** 276–285.

Huang, J.L. & Zhao, D.P., 2006. High-resolution mantle tomography of China and surrounding regions, *J. geophys. Res.,* **111,** doi:10.1029/2005jb004066.

Ito, E. & Takahashi, E., 1989. Postsphinel transformations in the system Mg_2SiO_4-Fe_2SiO_4 and some geophysical implicaitons, *J. geophys. Res.,* **94,** 10 637–10 646.

Jacobsen, S. & Smyth, J., 2006. Effect of water on the sound velocities of ringwoodite in the transition zone, *Geophys. Monogr.,* **168,** 131–145.

Jacobsen, S.D., Smyth, J.R., Spetzler, H., Holl, C.M. & Frost, D.J., 2004. Sound velocities and elastic constants of iron-bearing hydrous ringwoodite, *Phys. Earth planet. Inter.,* **143–144,** 47–56.

Karato, S.-I., 2011. Water distribution across the mantle transition zone and its implications for global material circulation, *Earth planet. Sci. Lett.,* **301,** 413–423.

Kennett, B.L.N. & Engdahl, E.R., 1991. Traveltimes for global earthquake location and phase identification, *Geophys. J. Int.,* **105,** 429–465.

Li, X.Q. & Yuan, X.H., 2003. Receiver functions in northeast China: implications for slab penetration into the lower mantle in northwest Pacific subduction zone, *Earth planet. Sci. Lett.,* **216,** 679–691.

Li, J., Chen, Q.F., Vanacore, E. & Niu, F.L., 2008. Topography of the 660-km discontinuity beneath northeast China: implications for a retrograde motion of the subducting Pacific slab, *Geophys. Res. Lett.,* **35,** doi:10.1029/2007GL031658.

Litasov, K., Ohtani, E., Sano, A., Suzuki, A. & Funakoshi, K., 2005. In situ X-ray diffraction study of post-spinel transformation in a peridotite mantle: implication for the 660-km discontinuity, *Earth planet. Sci. Lett.,* **238,** 311–328.

Miller, M.S., Kennett, B.L.N. & Toy, V.G., 2006. Spatial and temporal evolution of the subducting Pacific plate structure along the western Pacific margin, *J. geophys. Res.,* **111,** doi:10.1029/2005jb003705.

Niu, F. & Kawakatsu, H., 1996. Complex structure of mantle discontinuities at the tip of the subducting slab beneath northeast China: a preliminary investigation of broadband receiver functions, *J. Phys. Earth,* **44,** 701–712.

Schmerr, N. & Garnero, E.J., 2007. Upper mantle discontinuity topography from thermal and chemical heterogeneity, *Science,* **318,** 623–626.

Tajima, F. & Grand, S.P., 1995. Evidence of high-velocity anomalies in the transition zone associated with southern Kurile subduction zone, *Geophys. Res. Lett.,* **22,** 3139–3142.

Tajima, F. & Grand, S.P., 1998. Variation of transition zone high-velocity anomalies and depression of 660 km discontinuity associated with subduction zones from the southern Kuriles to Izu-Bonin and Ryukyu, *J. geophys. Res.,* **103,** 15 015–15 036.

Tajima, F., Katayama, I. & Nakagawa, T., 2009. Variable seismic structure near the 660 km discontinuity associated with stagnant slabs and geochemical implications, *Phys. Earth planet. Inter.,* **172,** 183–198.

Van Der Hilst, R., Engdahl, R., Spakman, W. & Nolet, G., 1991. Tomographic imaging of subducted lithosphere below northwest Pacific Island arcs, *Nature,* **353,** 37–43.

Wang, B. & Niu, F., 2010. A broad 660 km discontinuity beneath northeast China revealed by dense regional seismic networks in China, *J. geophys. Res.,* **115,** B06308, doi:10.1029/2009JB006608.

Wang, R., 1999. A simple orthonormalization method for stable and efficient computation of Green's functions, *Bull. seism. Soc. Am.,* **89,** 733–741.

Wang, T. & Chen, L., 2009. Distinct velocity variations around the base of the upper mantle beneath northeast Asia, *Phys. Earth planet. Inter.,* **172,** 241–256.

Wang, Y., Wen, L.X., Weidner, D. & He, Y.M., 2006. SH velocity and compositional models near the 660-km discontinuity beneath South America and northeast Asia, *J. geophys. Res.,* **111,** doi:10.1029/2005jb003849.

Widiyantoro, S., Kennett, B. & Van Der Hilst, R., 1999. Seismic tomography with P and S data reveals lateral variations in the rigidity of deep slabs, *Earth planet. Sci. Lett,* **173,** C91–C100.

Zheng, X.F., Yao, Z.X., Liang, J.H. & Zheng, J., 2010. The role played and opportunities provided by IGP DMC of China National Seismic Network in Wenchuan earthquake disaster relief and researches, *Bull. seism. Soc. Am.,* **100,** 2866–2872.

SUPPORTING INFORMATION

Additional Supporting Information may be found in the online version of this article:

Supplements S1–S3.
Figure S1. Relocation of the focal depth
Figures S2–S6. Forward modeling of SH triplicate waveforms
Figure S7. Comparison of previous regional models
Figure S8. Comparison of observed vertical *P*-wave displacements and synthetic waveforms

Please note: Wiley-Blackwell are not responsible for the content or functionality of any supporting materials supplied by the authors. Any queries (other than missing material) should be directed to the corresponding author for the article.

Supporting Information supplement for `A stagnant slab in a water-bearing mantle transition zone beneath northeast China: Implications from regional SH waveform modeling' by Lingling Ye, Juan Li, Tai-Lin Tseng and Zhenxing, Yao

1. Relocation of the focal depth

Precision of the focal depth is important in waveform modeling. There is a trade-off between event location and depth of the discontinuity. To minimize the uncertainty caused by focal depth, we relocated the earthquake by manually picked the P and pP arrival times from 330 teleseismic broadband records from IRIS (Incorporated Research Institute for Seismology). The misfit of pP–P travel times, based on iasp91 model, reaches a minimum at the depth of 519 km (Fig. S1). The minimum time residual is ~0.22 s with a standard deviation ~0.28 s, corresponding to a ~3 km uncertainty in the focal depth, and ~ ±0.15 s on the arrival time of triplicated phases.

2. Forward Modeling of SH Triplicate Waveforms

2.1 Evidence of high velocity anomaly above the 660

The striking feature of the AB branch extending to 25° in contrast to ~ 20° in Miasp, can be considered in two issues: a depressed 660 or a very gentle SH velocity gradient just above the 660. For the former case, we increased the depth of discontinuity from 660 km to 690 km (`model 1' in Fig. S3), however, this only shifts the location of O to a larger epicentral distance and the AB branch remains too short to fit the data (Fig. S3a). On the other hand, by introducing a high velocity layer with a very gentle gradient (~0.8 (m/s)/km) with thickness ~60 km at the bottom of MTZ, we can match the disappearing distance of the AB branch well (Fig. S3b). We also noticed a slight bending of move out of the AB branch at ~15° with the turning depth ~ 550 km, implying a velocity slope change might occur around here (`model 2' in Fig. S3c). In the next step, we will try to match the delayed travel-time by further

perturbing `model 2'.

2.2 Evidence of a low-SH-velocity MTZ

We noticed in Fig. S3 that the predicted AB phase is obviously earlier, and the time interval between the CD and AB phases is significantly narrow after the crossover of the two branches, in contrast to the observed `broad BOD'. This tendency can be considered either by increasing the velocity below the 660 or reducing the velocity in the MTZ. We kept the above detected feature of a high velocity layer with a very low gradient, and introduced a new model with ~2 per cent velocity variation below the 660 (`model 4' in Fig. S4). This modification predicted earlier O and C cusps that disagree with the observed `broad BOD'. Thus, we attribute the observed feature of the `broad BOD' to a relatively slow velocity layer somewhere in the MTZ. We noticed in Fig. S4a that, with the increasing of epicentral distance, as the rays sweep from the shallow MTZ to the bottom, the time residual of AB phases is much larger than that of CD phase. We thus speculate that a relatively low-shear-velocity MTZ, as shown in our preferred model `NEChina_S', is reasonable for the observed features. Although a simple model without the high velocity layer above the 660 but with the same velocity slope through the whole MTZ (`model 5' in Fig. S5) seems to improve the separation time between AB and CD phases, it fails to predict the observed extension of B cusp (Fig. S5a). Based on the above speculation, a combination of low velocity in MTZ and a relatively high anomaly structure just above the 660 (as `model 6') is necessary in generating the observed features as demonstrated in Fig. S5b.

2.3 Evidence of a broad 660-km discontinuity

We noticed that the initial point of the CD branch appears at a larger distance than predicted based on both models of iasp91 (Fig. 2a) and `model6' (Fig. S6). Since the emerging distance of C cusp is largely dependent on the velocity changes just below the discontinuity, we modified the step-like 660-km discontinuity to a broad one with thickness ~35 km (`NEChina_S' in Fig. S6b), which not only improves the relative time between AB and CD phases, but also the amplitude ratio between them as well. The same structure is also detected in our waveform modeling of P triplication, which is first proposed by Wang & Niu (2010).

3. Forward Modeling of P Triplicate Waveforms

To characterize the variation of Poisson's ratio in this region, we go through another round of P-wave analysis using the same pair of station-event geometry as in the S-wave study. The observed waveforms show two major features (Fig. S8a): (1) the CD phase doesn't show up until ~15° in contrast to ~12° in the iasp91 model; and (2) the AB branch terminates ~25°, extending far beyond the distance ~21° of the B-cusp of in iasp91 model. We followed the modeling process described in Wang and Niu (2010), and our preferred P velocity model `NEChina_P' (Fig. S8c) is nearly identical to that of Wang and Niu (2010), despite one minor difference in the sharpness of the 660. The thickness of the broad 660-km discontinuity in model `NEChina_P' is ~15 km thinner than that of their preferred model `255–270'.

References

Tajima, F., and S. P. Grand (1995), Evidence of High-Velocity Anomalies in the Transition Zone Associated with Southern Kurile Subduction Zone, *Geophys. Res. Lett.*, **22**(23), 3139–3142.

Wang, B., and F. Niu (2010), A broad 660-km discontinuity beneath northeastern China revealed by dense regional seismic networks in China, *J. geophys. Res.*, **115**, B06308, doi:10.1029/2009JB006608.

Wang, T., and L. Chen (2009), Distinct velocity variations around the base of the upper mantle beneath northeast Asia, *Phys. Earth Planet. Inter.*, **172**(3-4), 241-256.

Wang, Y., L. X. Wen, D. Weidner, and Y. M. He (2006), SH velocity and compositional models near the 660-km discontinuity beneath South America and northeast Asia, *J. geophys. Res.*, **111**(B7), doi:10.1029/2005jb003849.

Fig. captions

Figure S1. Variation of pP–P differential time residuals of the observation and predicted travel time from iasp91 along with the assumed hypocentral depth. The residual reaches to minimum at the depth ~ 519 km. Each error bar marks the maximum and minimum values of pP–P differential time residual among 330 stations estimated for a given hypocentral depth.

Figure S2. Comparisons of observed transverse displacements (black lines) and synthetic waveforms calculated using models: (a) iasp91 (dashed lines) and (b) Miasp with the shallow structure modified (dashed lines). The new generated model Miasp significantly improves the consistency in absolute times. However, about 1s of time delay remains unexplained. The two numbers at the right side of each waveform in (b) represent the name and azimuth angle of each station. (c) Comparison of the shear velocity models of iasp91 and Miasp.

Figure S3. Comparisons of observed transverse displacements (black lines) and synthetic waveforms calculated using models: (a) `model 1′ with the 660 depressed to 690 km (dashed lines) and (b) `model 2′ with a high velocity anomaly in the deeper part of the MTZ and a gentle velocity gradient just above the 660 (dashed lines). (c) Comparison of the shear velocity models of `model 1′, `model 2′ and iasp91. Other captions are same as those in Fig. S2.

Figure S4. Comparisons of observed transverse displacements (black lines) and synthetic waveforms calculated using two models modified from `model 2′: (a) `model 3′ with slower velocity in the upper part of the MTZ (dashed lines) and (b) `model 4′ with a ~ 2 per cent faster $V_S$ below the 660 (dashed lines). (c) Comparison of the shear velocity models of `model 3′, `model 4′ and iasp91. Other captions are same as those in Fig. S2.

Figure S5. Comparisons of observed transverse displacements (black lines) and synthetic waveforms calculated using models: (a) `model 5′ with a slower velocity (~1 per cent) in the entire MTZ (dashed lines) and (b) `model 6′ modified from `model 5′ by adding a high velocity anomaly in the deeper part of the MTZ with a gentle velocity gradient just above the 660 (dashed lines). (c) Comparison of the shear velocity models of `model 5′, `model 6′ and iasp91. Other captions are same as those in Fig. S2.

Figure S6. Comparisons of observed transverse displacements (black lines) and synthetic waveforms calculated using models: (a) `model 6′ (dashed lines) and (b) our preferred model `NEChina_S′, in which a broad 660-km discontinuity with thickness ~35km is introduced (dashed lines). (c) Comparison of the shear velocity models of `model 6′, `NEChina_S′ and iasp91. Other captions are same as those in Fig. S2.

Figure S7. (a) Comparison of previous regional models: `M3.11′ (Tajima and Grand, 1995), `255–270′ (Wang and Niu, 2010), `Asia′ (Wang et al., 2006), `Japan′ (Wang and Chen, 2009) and our preferred model `NEChina_S′. Models `M3.11′ and `255–270′ are derived from P wave modeling, and we converted them to shear velocity model using associated P-to-S velocity ratio of iasp91. (b) Predicted travel times of triplicated phases from different models. The dots indicate the observed peak time for AB and CD phases.

Figure S8. Comparisons of observed vertical P-wave displacements (black lines) and synthetic waveforms calculated using models: (a) iasp91 (dashed lines) and (b) our preferred model `NEChina_P′, in which a high velocity anomaly in the deeper part of the MTZ and a broad 660-km discontinuity with thickness ~35 km is introduced (dashed lines). (c) Comparison of the P velocity models of `NEChina_P′and iasp91. Station corrections of ~1.0 s are made for stations located within epicentral distance of 18°–22°, which might be related with the local structure beneath stations. Other captions are same as those in Fig. S2.

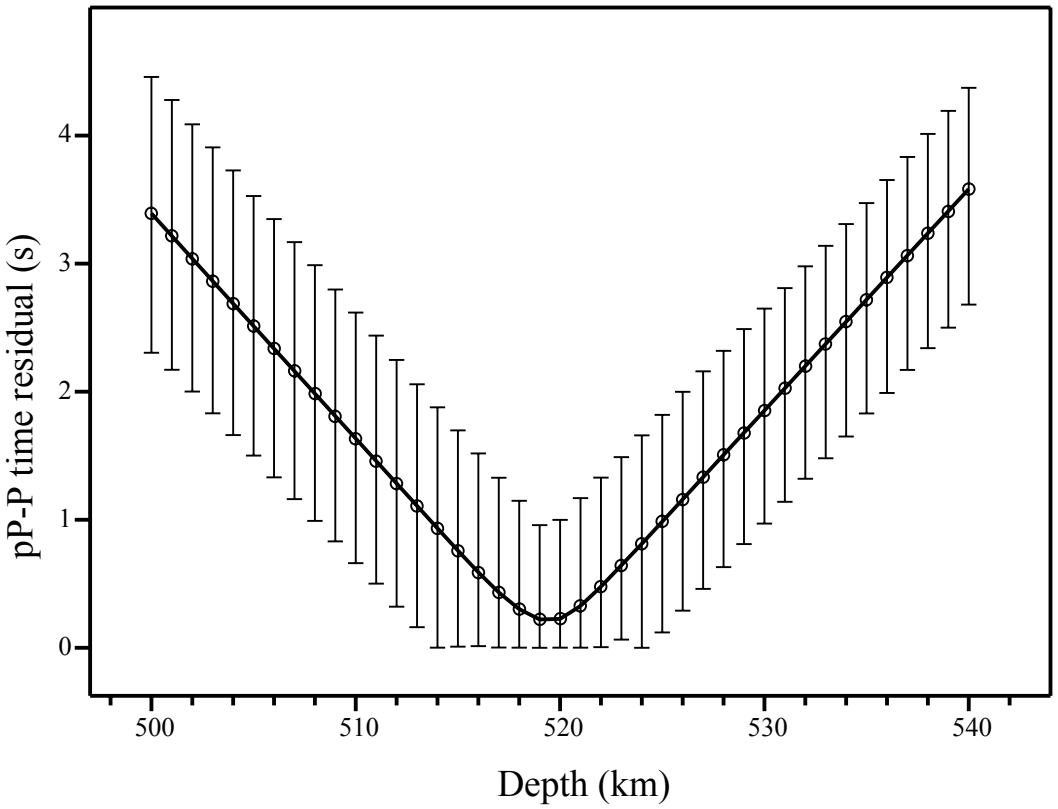

Figure S1

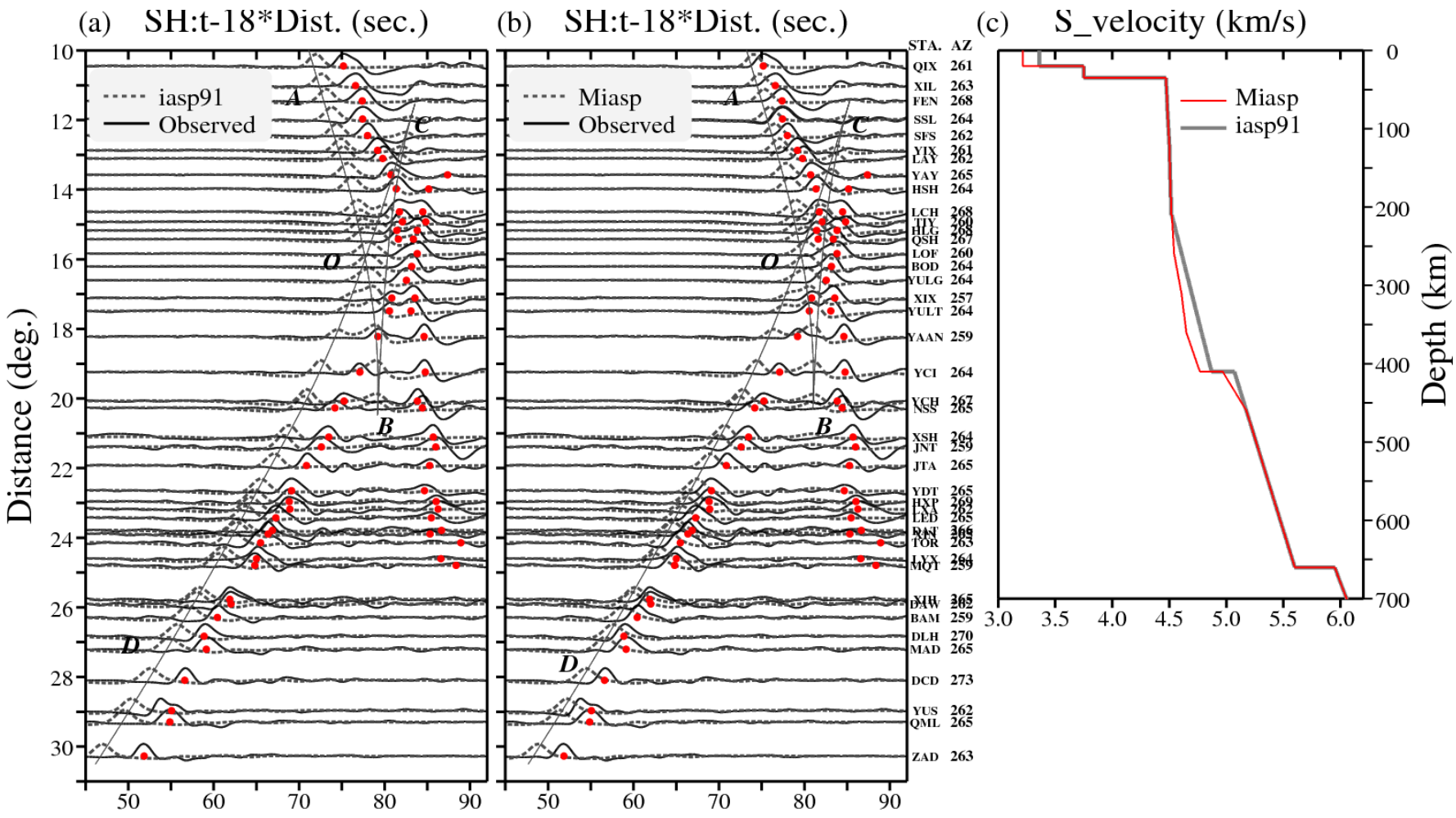
(a) SH:t-18*Dist. (sec.)
(b) SH:t-18*Dist. (sec.)
(c) S_velocity (km/s)
iasp91
Observed
Miasp
Observed
Miasp
iasp91
Distance (deg.)
Depth (km)
A
B
C
D
O
STA. AZ
QIX 261
XIL 263
FEN 268
SSL 264
SFS 262
YIX 261
LAY 262
YAY 265
HSH 264
LCH 268
TTY 260
HLG 268
QSH 267
LOF 260
BOD 264
YULG 264
XIX 257
YULT 264
YAAN 259
YCI 264
YCH 267
NSS 265
XSH 264
JNT 259
JTA 265
YDT 265
HXP 269
LED 265
TOR 263
MQI 259
DAW 262
BAM 259
DLH 270
MAD 265
DCD 273
YUS 262
QML 265
ZAD 263

Figure S2

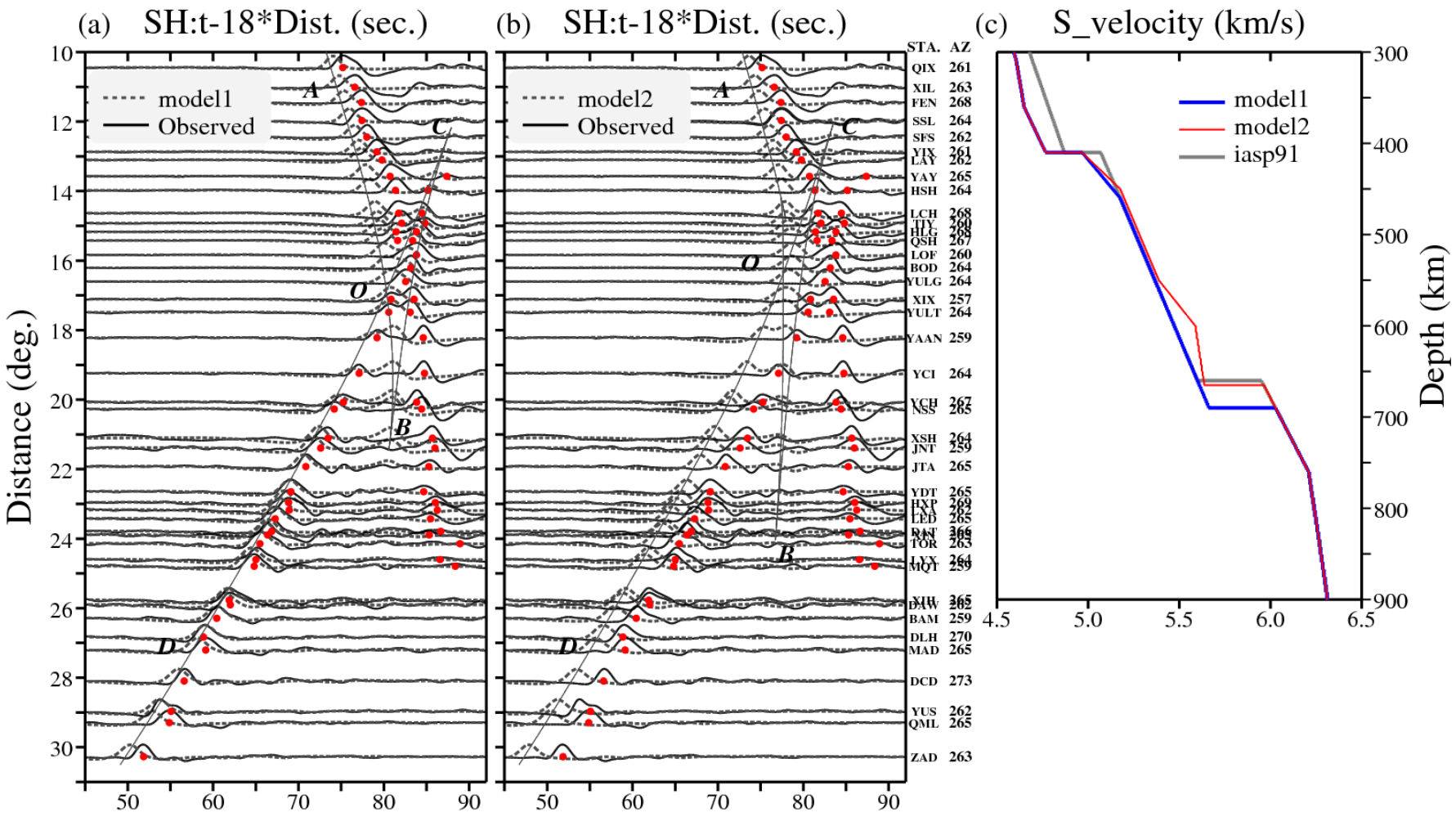
(a) SH:t-18*Dist. (sec.)
(b) SH:t-18*Dist. (sec.)
(c) S_velocity (km/s)
model1
Observed
model2
Observed
model1
model2
iasp91
Distance (deg.)
Depth (km)
A
B
C
D
STA. AZ
QIX 261
XIL 263
FEN 268
SSL 264
SFS 262
YAY 265
HSH 264
LOF 260
BOD 264
YULG 264
XIX 257
YULT 264
YAAN 259
YCI 264
XSH 264
JNT 259
JTA 265
YDT 265
LED 265
TOR 263
DLH 270
MAD 265
DCD 273
YUS 262
QML 265
ZAD 263

Figure S3

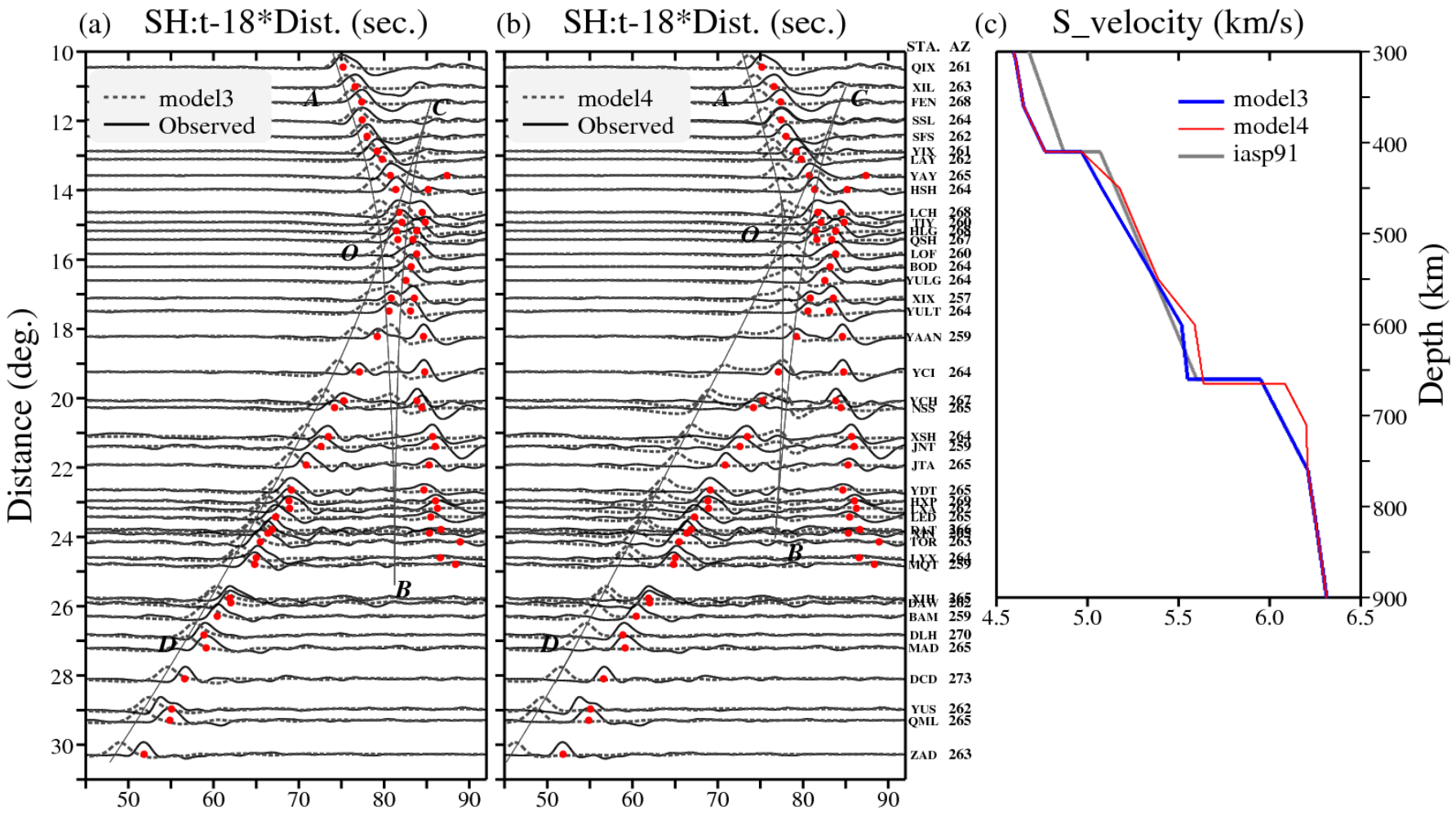
(a) SH:t-18*Dist. (sec.)
(b) SH:t-18*Dist. (sec.)
(c) S_velocity (km/s)
model3
Observed
model4
Observed
model3
model4
iasp91
Distance (deg.)
Depth (km)
STA. AZ
A
B
C
D
O

Figure S4

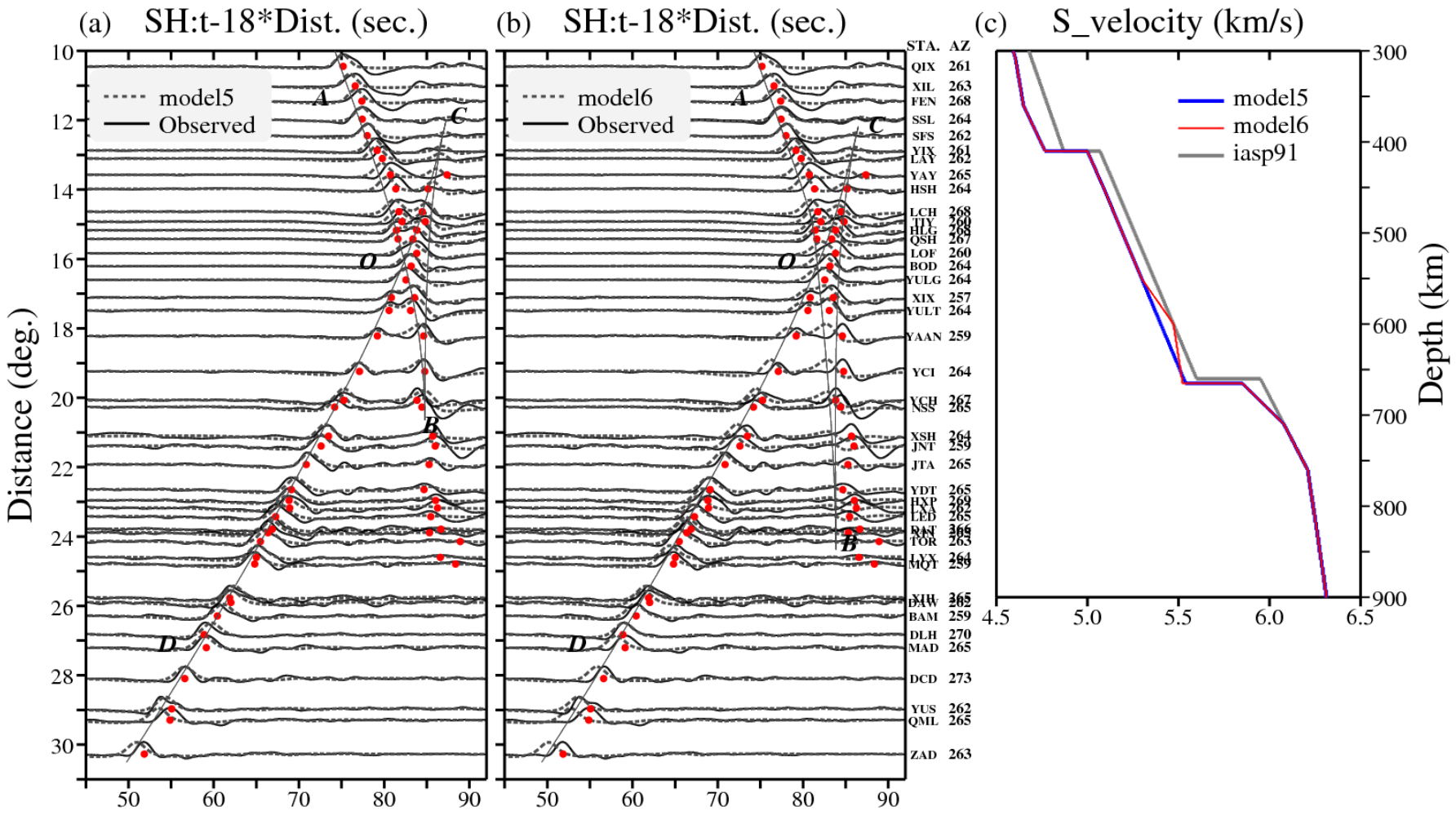
(a) SH:t-18*Dist. (sec.)
(b) SH:t-18*Dist. (sec.)
(c) S_velocity (km/s)
model5
Observed
model6
Observed
model5
model6
iasp91
Distance (deg.)
Depth (km)
A
B
C
D
O
STA. AZ
QIX 261
XIL 263
FEN 268
SSL 264
SFS 262
XIX 261
LAY 262
YAY 265
HSH 264
LCH 268
JIY 260
HLG 266
QSH 267
LOF 260
BOD 264
YULG 264
XIX 257
YULT 264
YAAN 259
YCI 264
YCH 267
NSS 265
XSH 264
JNT 259
JTA 265
YDT 265
HXP 269
LXA 262
LED 265
TOR 263
LYX 264
MQI 259
DAW 262
BAM 259
DLH 270
MAD 265
DCD 273
YUS 262
QML 265
ZAD 263

Figure S5

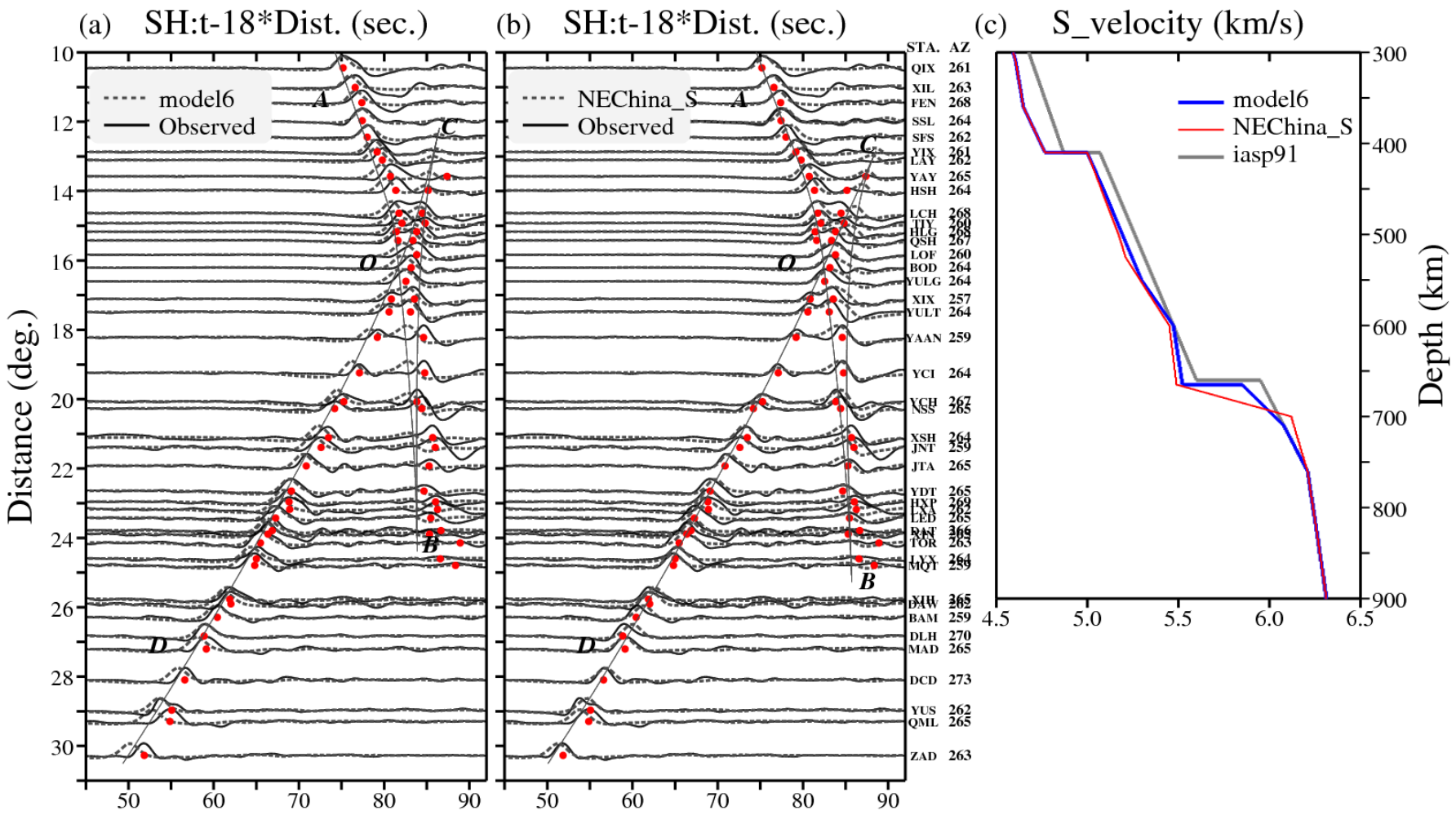
(a) SH:t-18*Dist. (sec.)
(b) SH:t-18*Dist. (sec.)
(c) S_velocity (km/s)
model6
Observed
NEChina_S
Observed
model6
NEChina_S
iasp91
Distance (deg.)
Depth (km)
STA. AZ
QIX 261
XIL 263
FEN 268
SSL 264
SFS 262
YAY 265
HSH 264
LCH 268
QSH 267
LOF 260
BOD 264
YULG 264
XIX 257
YULT 264
YAAN 259
YCI 264
XSH 264
JNT 259
JTA 265
YDT 265
LED 265
TOR 263
BAM 259
DLH 270
MAD 265
DCD 273
YUS 262
QML 265
ZAD 263
A
B
C
D

Figure S6

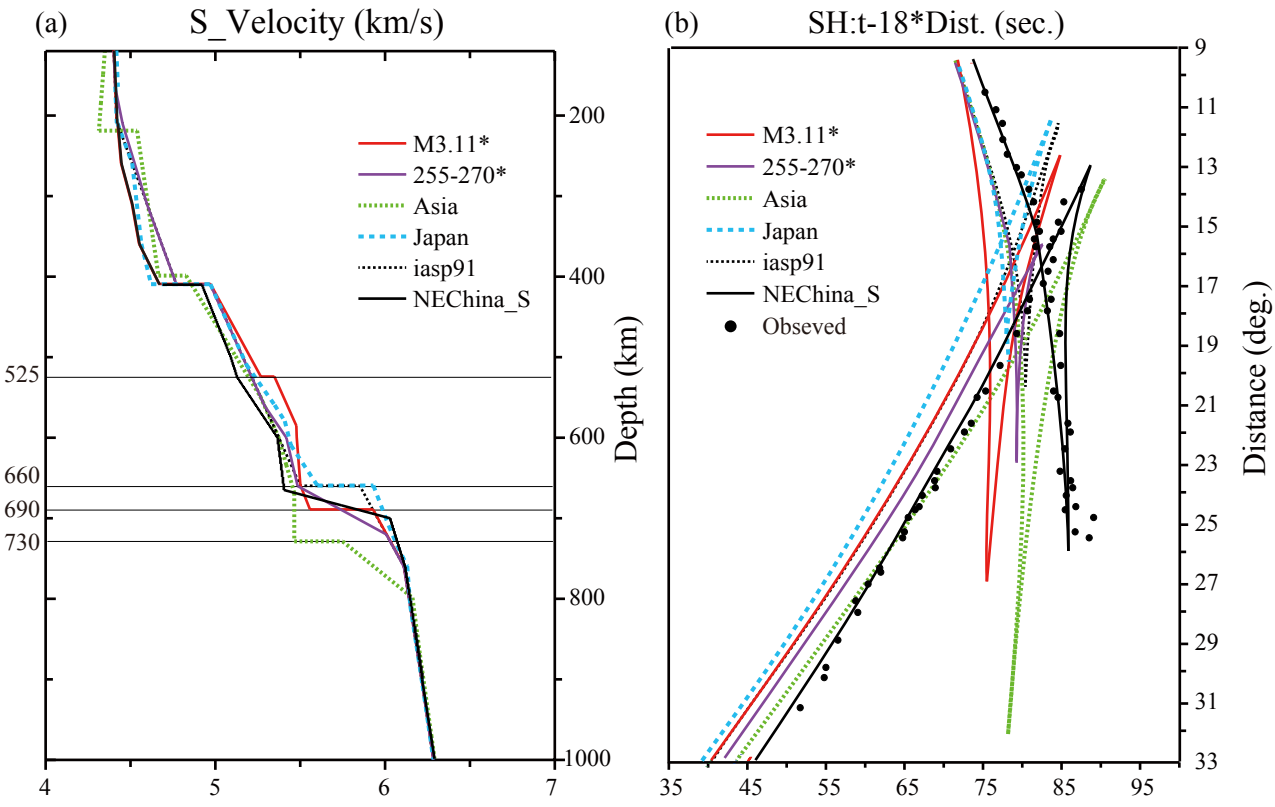
(a)
S_Velocity (km/s)
M3.11*
255-270*
Asia
Japan
iasp91
NEChina_S
525
660
690
730
Depth (km)
(b)
SH:t-18*Dist. (sec.)
Obseved
Distance (deg.)

Figure S7

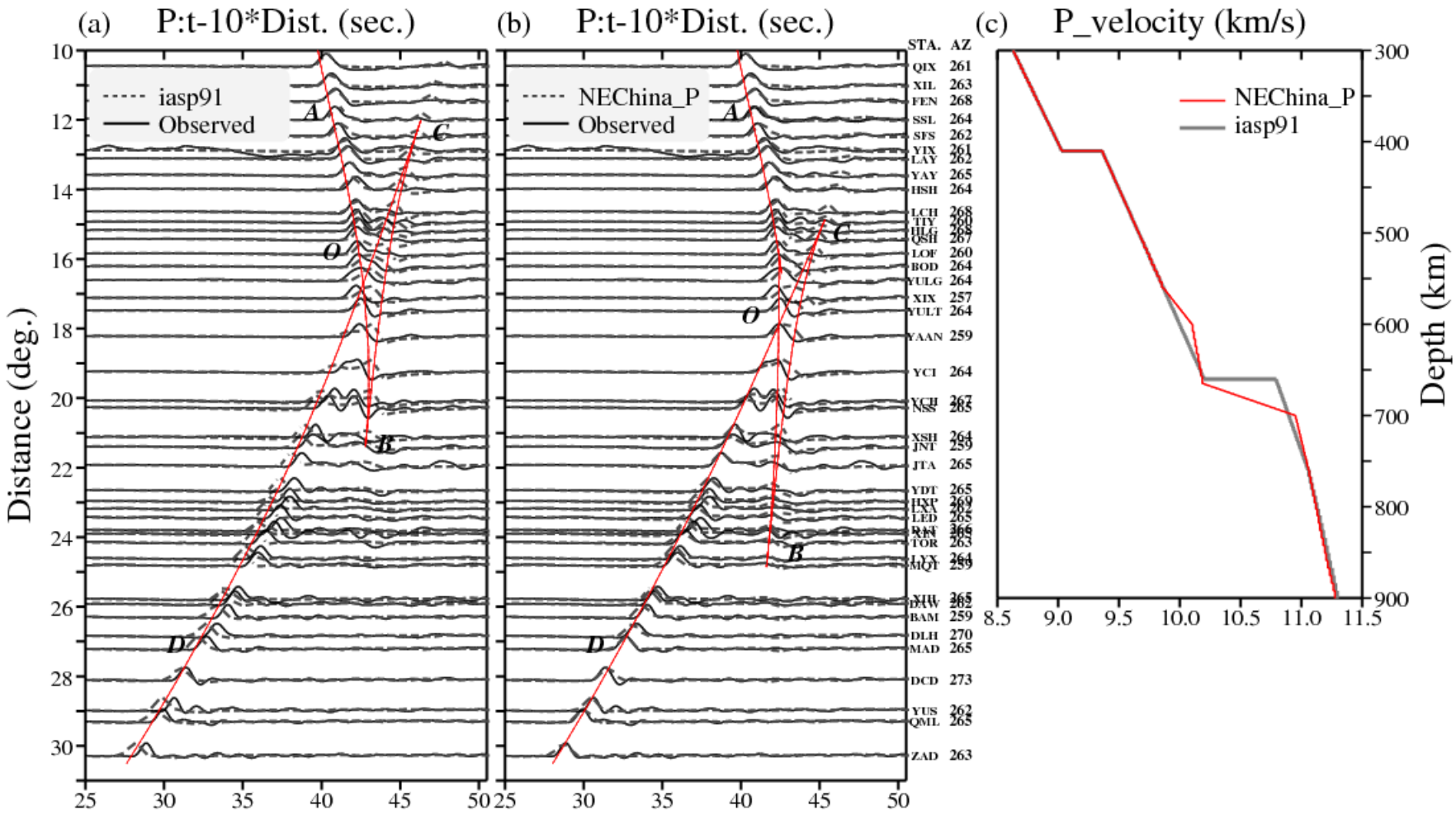
(a) P:t-10*Dist. (sec.)
(b) P:t-10*Dist. (sec.)
(c) P_velocity (km/s)
iasp91
Observed
NEChina_P
Observed
NEChina_P
iasp91
Distance (deg.)
Depth (km)
STA. AZ
A
B
C
D
O

Figure S8